Adsorption location of copper on hemp shives revealed by combination of K-edge subtraction X-ray microtomography and X-ray micro-fluorescence

Chiara Mongiovi, Xavier Gabrion, Jason Govilas, Wajih Akleh, Mario Scheel, Jonathan Perrin, Timm Weitkamp, Sylvie Durand, Léna Brionne, Camille Rivard, et al.

Adsorption location of copper on hemp shives revealed by combination of K-edge subtraction X-ray micro-tomography and X-ray micro-fluorescence

Chiara Mongioví, Xavier Gabrion, Jason Govilas, Wajih Akleh, Mario Scheel, Jonathan Perrin, Timm Weitkamp, Sylvie Durand, Léna Brionne, Camille Rivard, Sebastian Schöder, Katharina Müller, Johnny Beaugrand, Vincent Placet, Grégorio Crini

Chiara Mongioví, Grégorio Crini (✉)

Université de Franche-Comté, CNRS, Laboratoire Chrono-environnement, 16 route de Gray, 25000 Besançon, France

E-mail: gregorio.crini@univ-fcomte.fr, (G. Crini, ORCID: 0000-0003-2540-6851)

Xavier Gabrion

SUPMICROTECH, CNRS, Institut FEMTO-ST, Université de Franche-Comté, 25000 Besançon, France

Jason Govilas, Wajih Akleh, Vincent Placet

Department of Applied Mechanics, CNRS, Institut FEMTO-ST, Université de Franche-Comté, 25000 Besançon, France

Mario Scheel, Jonathan Perrin, Timm Weitkamp, Camille Rivard, Sebastian Schöder

Synchrotron SOLEIL, L'Orme des Merisiers, Départementale 128, 91190 Saint-Aubin, France

Camille Rivard

Synchrotron SOLEIL, L'Orme des Merisiers, Départementale 128, 91190 Saint-Aubin, France

TRANSFORM, UAR 1008, INRAE, Imp. Yvette Cauchois, 44300 Nantes, France

Sylvie Durand, Léna Brionne, Johnny Beaugrand

BIA, UR1268, INRAE, 44316 Nantes, France

Katharina Müller

IPANEMA, UAR 3461 CNRS, site du Synchrotron SOLEIL, 91190 Saint-Aubin, France

Abstract In the literature, hemp shives have been proposed as adsorbents capable of effectively complexing metals in aqueous solution. However, studies on the localization of metals in these multicell type lignocellulosic materials are scarce and further description of adsorption sites are required for better optimization of adsorbent capacity. In this article, we show the complementarity of two synchrotron-radiation techniques, namely K-edge subtraction micro-tomography and X-ray micro-fluorescence, to visualize the spatial distribution of the copper complexed by hemp shives. Three materials have been studied: a sample washed in water (SHI-W), a sample activated using sodium carbonate (SHI-C), and a sample chemically modified by 1,2,3,4-butanetetracarboxylic acid in order to introduce carboxylic groups (SHI-BTCA). Tomography provides 3D information and only locates areas where copper is present in significant proportions. X-ray fluorescence imaging allows for a lower detection limit, but only provides 2D information. Data analysis confirmed that the Cu distribution is totally different for the three samples, in agreement with the proposed adsorption mechanism: adsorption surface and diffusion for SHI-W and SHI-C and chemisorption and ion-exchange for SHI-BTCA.

Keywords *Hemp shives . Copper . Adsorption . X-ray micro-fluorescence . K-edge subtraction imaging . XRF mapping*

Graphical abstract

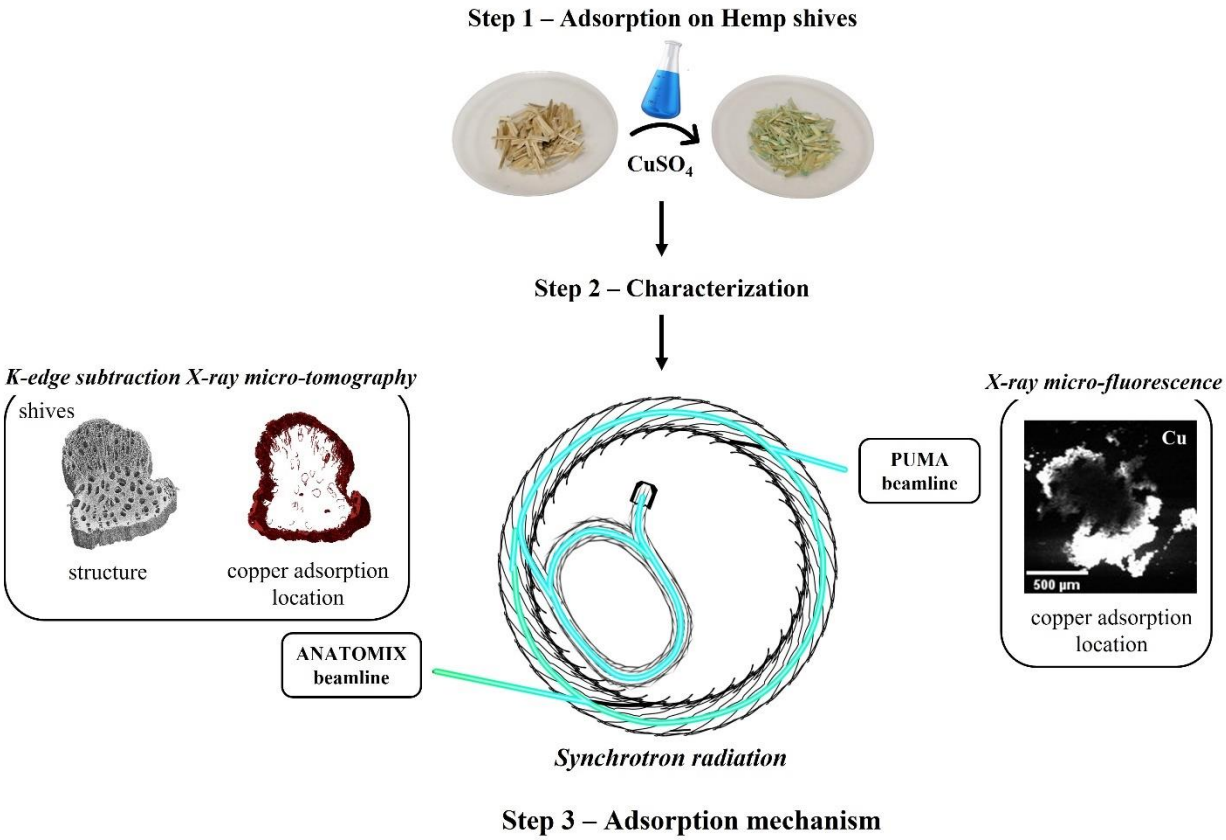

Introduction

In the field of water treatment, by-products of agricultural origin and from forest industries are proposed as adsorbents for metal removal using adsorption-oriented processes. These natural materials are lignocellulosic complexes mainly consisting of cellulose, hemicelluloses and lignin and showing appropriate adsorption properties due to their multicomponent composition, particular structure, and the presence of various actives ligands. The main advantages of adsorption using by-products of agricultural origin are the availability of the raw materials, the simple operation, cheapness of the processes, high efficiency in metal removal, and easy elimination of spent materials by incineration (Halysh et al. 2020; Sjahro et al. 2021; Sharma et al. 2022).

The adsorbents proposed are, for example, sugarcane bagasse, corn cobs, corn stalks, coir, jute, date pits, rice straw, fruit peel waste, walnut shells, shells of almond, cotton waste, bark, sawdust, flax, hemp, and cellulose nanocrystals (Junior et al. 2012; Asberry et al. 2014; de Quadros Melo et al. 2016; Furlan et al. 2018; Morin-Crini et al. 2019; Shen et al. 2019; Wang 2019; Halysh et al. 2020; Mokgehle et al. 2021; Santander et al. 2021; Sjahro et al. 2021; Ahmed et al. 2022; Basnet et al. 2022; Cruz-Lopes et al. 2022; Mergbi et al. 2023; Akköz and Coşkun R 2023; Pinsard et al. 2023; Zeng et al. 2023). They are used both in raw and modified form and in particles (shives), fibers, felts and powder forms. Indeed, chemical modification can improve the adsorption properties of the materials (Lee and Rowell 2004; Chandraghatgi and Englezos 2008; Sjahro et al. 2021). Regarding hemp, some studies concluded that hemp-based materials could be low-cost and viable

adsorbent for metal removal (Morin-Crini et al. 20219; Pinsard et al. 2023). Empirical mathematical models are often used to fit the adsorption experimental data and to draw conclusions, from the assumptions of these models, in order to identify the interactions involved in the liquid-solid adsorption mechanism (Halysh et al. 2020). Another complementary and necessary approach is to couple different microscopic and spectroscopic techniques to obtain information on these mechanisms. For example, to characterize materials before and after use, techniques such as scanning electron microscopy (SEM), energy-disperse X-ray (EDX), Fourier transform infrared spectroscopy (FTIR), Raman spectroscopy, X-ray photoelectron spectroscopy (XPS), X-ray absorption near-edge structure (XANES) spectroscopy, computed micro-tomography (micro-CT), and density functional theory (DFT) calculations are used. These techniques can provide information on the type of functional groups present in the materials, their distribution in the structure, and their role and involvement in the adsorption mechanism (Biziks et al. 2016; Jiang et al. 2017, 2018; Mongioví and Crini 2023; Mongioví et al. 2021, 2022a, 2022b; Sun et al. 2021; Müller et al. 2021; Maceda et al. 2022; da Rocha Rodrigues et al. 2023). Information on the precise location of the distribution of metals in materials is however rare.

Since the last decade, hemp-based materials in felt and shives forms, as co-products of the hemp industry, have also been proposed by our research group as low-cost, available and efficient adsorbents for the complexation of various metals, e.g., Al, Co, Cu, Mn, Ni and Zn, present in aqueous solutions (Crini et al. 2021; Morin-Crini et al. 2020). These materials had high adsorption capacities towards metals depending mainly on the type of material used. A recent study revealed the adsorption mechanism of materials prepared from hemp shives, namely sodium carbonate-activated (SHI-C) and polycarboxylic agent-grafted (SHI-BTCA) hemp shives, using microscopic and spectroscopic techniques (Mongioví et al. 2022b). The main difference between the two materials is the amount of carboxylate groups, which is much higher in the case of the SHI-BTCA sample. The combination of the SEM, EDX, FTIR, Raman, XANES, and XPS techniques allowed us to characterize and distinguish the type of interactions involved in the liquid-solid adsorption phenomena for copper complexation by each sample. The results showed that the Cu adsorption mechanisms on the hemp shives SHI-C and SHI-BTCA were remarkably different. For the first adsorbent, surface adsorption of copper and diffusion into the structure of the material were predominant, whereas for the second material, copper adsorption was due to chemisorption (microprecipitation, complexation) and ion exchange, highlighting in the latter case the main role of carboxylate groups.

In this work, the location of copper adsorbed on the hemp shives was studied thanks to a combination of two synchrotron techniques, namely K-edge subtraction X-ray micro-tomography (KES tomography) and X-ray micro-fluorescence imaging, to better understand mechanisms involved during the copper adsorption.

Materials and methods

Materials

Hemp shives or also called Chènevotte, abbreviated SHI, were provided by Eurochanvre (Arc-les-Gray, France), an agricultural cooperative. These commercial shives (0.12-0.9 euros/kg depending of the quality) (Pinsard et al. 2023) are constituted by parallelepiped

particles whose length varies from 5 up to 25 mm (Figure 1), being commercialized for plant and animal mulching, and insulation. In this work, three materials have been studied: a sample washed in water (abbreviated SHI-W), a sample activated using sodium carbonate (SHI-C), and a sample chemically modified by 1,2,3,4-butanetetracarboxylic acid in order to introduce carboxylic groups (SHI-BTCA). These modifications have been recently detailed (Mongioví and Crini 2023; Mongioví et al. 2021, 2022a, 2022b). The results showed significant changes in the surface morphology of each sample after treatment and their chemical composition. Briefly, for SHI-W, the washing eliminated water-soluble components. Alkaline treatment (SHI-C) increased the percentage of cellulose and reduced the ratio of hemicelluloses. When compared to the hemicellulose content, the amount of lignin did not vary. SHI-BTCA sample showed a completely different chemical composition due the grafting reaction. The volume of the pores, obtained from micro-tomography measurements, was comparable for all the washed and activated samples, while for the grafted sample a significant decrease was observed. However, for this later material, the grafting with BTCA led to an important increase in the ionic exchange capacity values due to the presence of carboxylic groups. SHI-W, SHI-C and SHI-BTCA samples were used as adsorbents for the adsorption of copper present in solutions using the batch method previously detailed (Mongioví and Crini 2023). In this work, experimental batch protocol is the following: 2 g of shives were added to 100 mL of copper solution (at a concentration of 200 mg/L); the solution was stirred for 2 h and the shives were then recovered and directly frozen.

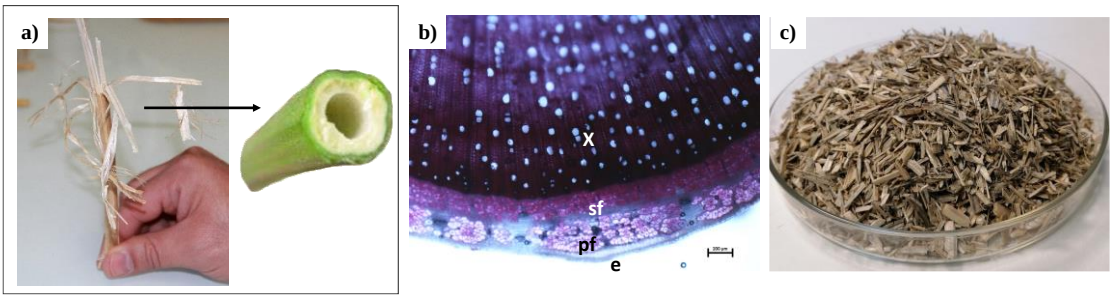

Fig. 1 Raw hemp shives: a) stem; b) stem cross-section (X: xylem; pf: primary fiber; sf: secondary fiber; e: epidermis); and c) shives

Preparation of samples for synchrotron measurements

Transverse and longitudinal cryo thin sections of the shives were prepared using a cryomicrotome (CM 3050S, Leica, Nanterre). The shives, before and after copper adsorption, were placed wet in moulds and coated with OCT (Optimal Cutting Temperature, VWR France). The samples in their moulds were then fast frozen by plunge in an isopentane solution cooled with liquid N_2. Several 20 µm thick sections were then collected from the sample blocks at different locations: longitudinal sections at the surface of the shives and transverse sections at two depths in the shives, one close to the surface and the other deeper. These sections were placed between two Ultralene films (SPEX SamplePrep) in a dedicated sample holder. Each section was observed under an optical microscope (AZ100M Macroscope, Nikon, Japan) prior to check its quality.

X-ray micro-fluorescence (XRF)

µ-XRF analysis was performed at the PUMA beamline of Synchrotron SOLEIL. A Si(111) double crystal monochromator (DCM) was used to monochromatize the beam and a Kirkpatrick-Baez (KB) mirror system focalized the X-rays on the surface of the samples in a diameter of 5 µm (vertical) and 10 µm (horizontal, including the footprint of the beam). The samples were mounted in a 45 degree geometry with the incoming beam, a silicon drift detector (RaySpec Ltd), placed at 90-degree geometry, was used to record the fluorescence spectra. A home-made diamond beam monitor was used to record the intensity of the primary beam (I0) at the exit of the KB mirror system. A video-microscope allowed to align the sample visually and to observe it during the acquisition. The cartographies of 10 µm x 5 µm were made with an incident X-ray beam energy of 10 keV and acquired in continuous scanning mode. A spatial resolution of 5, 7 or 10 µm was used. The obtained data were corrected for deadtime and I0 via a python script and then fitted with the PyMCA (ESRF) software package (Solé et al. 2007).

Micro-tomography

For this analysis, we chose shives with a dimension of approximatively 1 mm^2 in section and 10 mm length. K-edge subtraction tomograms were acquired at ANATOMIX beamline of Synchrotron SOLEIL (Weitkamp et al. 2022). The shive samples were mounted on the rotation stage; motorized XYZ translation stages were used to center the sample on the tomography rotation axis and align it with the field of view of the detector. The scans were conducted with an electron beam current of 500 mA in the storage ring. Using the Si(111) double-crystal monochromator of the beam-line (energy bandwidth $\Delta E/E \approx 10^{-4}$), the X-ray beam used for the measurements was set to photon energies of 8.975 and 9.003 keV for measurements, respectively, below and above the copper absorption edge. These energies were chosen using tabulated values from literature. To increase the X-ray flux density on the sample, a collimating compound refractive X-ray lens consisting of three biconcave beryllium lenses (RXOPTICS GmbH & Co. KG, Monschau, Germany) with a surface curvature radius of 1.0 mm in the apex and a circular aperture of 1.9 mm was inserted into the X-ray beam at a position 37 m from the X-ray source and 133 m from the sample position. The tomography data were recorded with an indirect detector system (Desjardins et al. 2018) consisting of a single-crystal lutetium aluminum garnet scintillator screen, a CMOS-based scientific-grade camera (Hamamatsu Orca Flash 4.0 V2) with 2048×2048 pixels (physical pixel size 6.5 µm) and microscope optics with a magnification of 10 (using an objective 10×/NA 0.28 from Mitutoyo) that projected the visible-light image from the scintillator onto the sensor of the camera, resulting in an effective pixel size of 0.65 µm and a field of view (FOV) of the detector of $(1.3\ mm)^2$. The exposure time was set to 20 ms per projection radiograph. In each tomography scan, 2000 projection radiographs were acquired on the fly (i.e., without stop of the rotating table between projections) over a scan range of 180 degrees.

The volume reconstruction was performed with the PyHST2 computer program (ESRF, Grenoble, France) (Mirone et al. 2014) at a voxel size of 0.65 µm; the reconstructed cylinder-shaped volumes have a diameter and height of 1.3 mm, corresponding to the detector FOV. To visualize the copper present in the shives, KES tomography was performed. The general principle is described in Figure 2. The same sample was irradiated by X-rays at two different energies around the copper K absorption edges as was already used with nanotomography (TXM instrument) at the ANATOMIX beamline (Scheel et al.

2014). The photoelectric absorption (i.e., attenuation) of X-rays by any chemical element increases abruptly as the X-ray photon energy is slightly increased from a value below the binding energy of electrons in a given electron shell of that element's atoms to a value just above that binding energy; the binding energy value is therefore also referred to as an "X-ray absorption edge" for that element. For Cu, the electron binding energy for the K shell (i.e., the 1s shell) is 8979 eV (Thompson et al. 2009). Acquiring two sets of X-ray image data, one below and one above this energy, results in different signals between both data sets only at those positions in the images where Cu is present. While both contain signal from the lignocellulosic material and the copper adsorbed on it, the copper signal is much stronger in the second type of images than in the first, while the signal from the lignocellulosic material is essentially identical for both types of images. By subtracting both types of images from one another, it was possible to isolate the copper signal (areas of high brightness) and obtain a third image showing only the spatial distribution of the metal (Figure 2). This method can detect the copper in the volume if the quantity is large. The post-processing of the KES tomography data was carried out using VG StudioMax 2023-1 and Fiji softwares. The two volumes were aligned with a best fit algorithm implemented in the software, and the subtraction method is applied (volume acquisition above Cu K-edge minus volume acquisition below Cu K-edge).

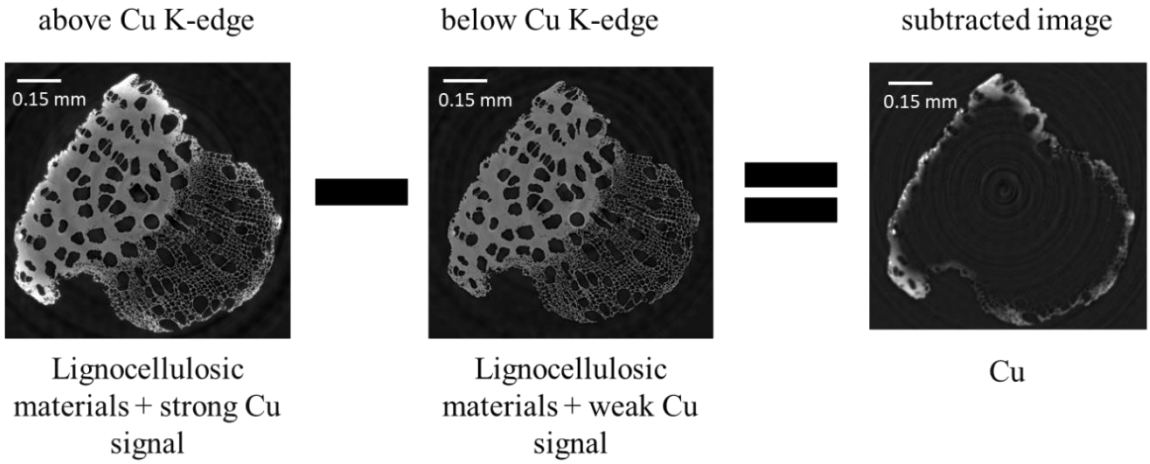

Fig. 2 K-edge subtraction micro-tomography virtual cross-sections of shives taken at photon energies above (left) and below Cu K-edge (middle) and resulting image after application of the subtraction method (right).

Results and discussion

The KES tomography images in Figure 3 compare the presence of Cu before and after adsorption for the SHI-BTCA sample. The absence of Cu before the metal adsorption process is clearly visible. Indeed, the slice from the volume data set acquired below the Cu K edge is very similar to the one taken above the edge. Consequently, the subtraction of grey level of the slice above threshold minus the slice below the Cu K-edge does not show any difference (other than ring artifacts from slight changes in the X-ray beam profile, i.e., induced by the instrument), which confirms that this specimen has not be exposed to copper (Figure 3a).

In contrast, the difference image from the SHI-BTCACu sample shows the presence of copper by high image intensity, highlighting the areas where copper is present (in white in Figure 3b, right). This brightness is mostly localized in areas near the surface of the sample. Similar results were obtained by analyzing the SHI-W and SHI-C samples, whose images are shown in Supplementary files.

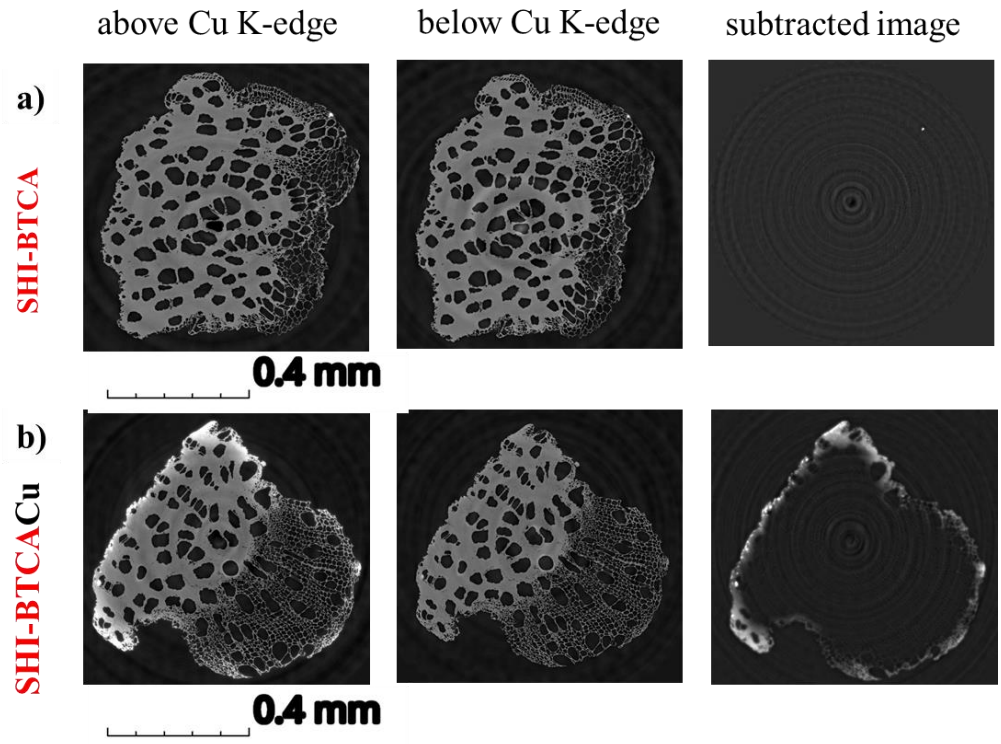

Fig. 3 Micro-tomography virtual cross-sections (slices) taken at X-ray photon energies above (left) and below the Cu K-edge (middle) and subtracted image (right) for the SHI-BTCA sample before (a) and after (b) copper adsorption.

Figure 4 compares 3D tomography images for SHI-WCu, SHI-CCu and SHI-BTCACu shives taken above the Cu K-edge with the resulting 3D images after application of the subtraction method. For SHI-WCu and SHI-CCu, the metal is localized both over the external and internal surfaces of the material (which is consistent with the assumption of a diffusion mechanism). In contrast, for SHI-BTCACu, copper is located mainly on the outer surface and around the surface of the vessels involving carboxylate functions, in agreement with recent data (Mongioví et al. 2022b).

For SHI-CCu, the copper is distributed in all the surface of the shives due to the partial removal of the hemicelluloses during sample activation (Mongioví et al. 2021). Indeed, the treatment with sodium carbonate induced in the cell wall some micro- and nano-porosities into which the aqueous solution can diffuse. So, for this sample, the mechanism of adsorption of the copper is completely different than that for SHI-BTCA.

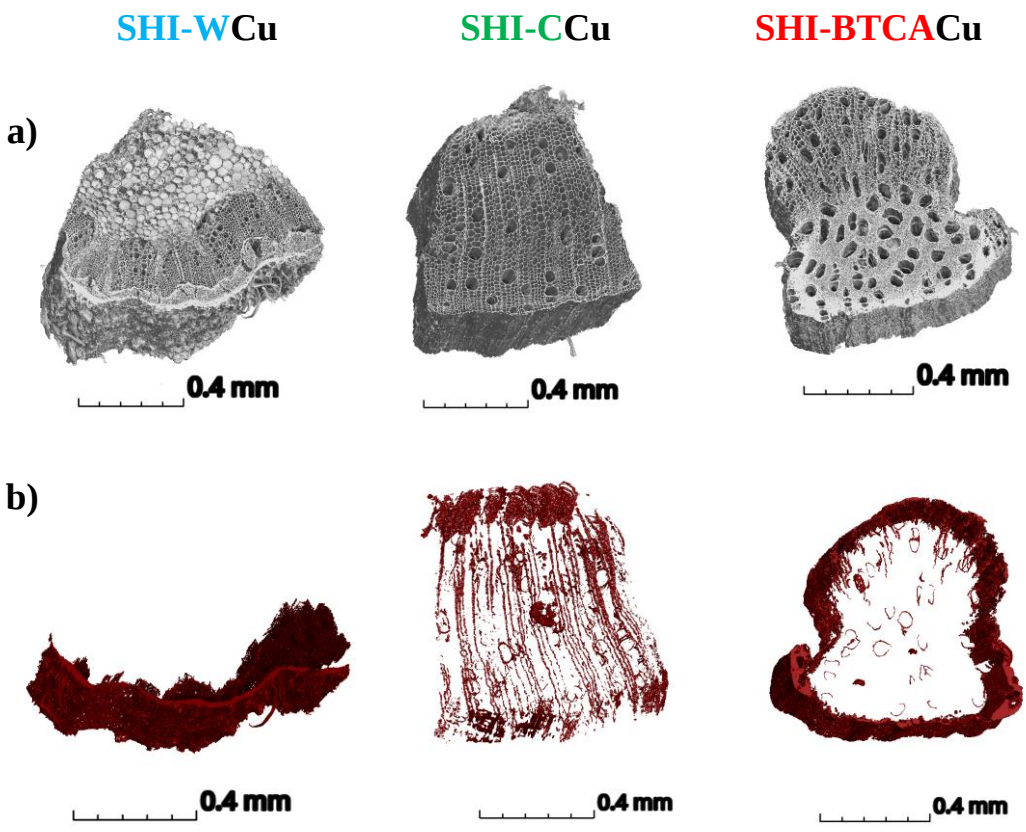

Fig. 4 3D K-edge subtraction tomography images for SHI-WCu, SHI-CCu and SHI-BTCACu shives after copper adsorption: a) above Cu K-edge and b) after application of the subtraction method.

To determine the spatial distribution of copper in hemp samples after adsorption, µ-XRF maps were also acquired. Elemental maps were extracted from the fluorescence spectra collected in each pixel. The abundance of each element is represented by a grayscale: the higher the intensity of the fluorescence signal, the brighter the image, and the more concentrated the element. For a given element, the same intensity scale was chosen on all maps in order to be able to compare them quantitatively. On the other hand, the grayscales chosen are not identical for the different elements because of the very different abundances. It is therefore not possible to directly compare the abundance of one element to that of another from these images. The XRF map of the shives before adsorption shows the presence of calcium, distributed over the entire sample, with accumulation in the pith area (Figure 5). No copper signal is visible on these maps, indicating its absence or the presence of a very low concentration.

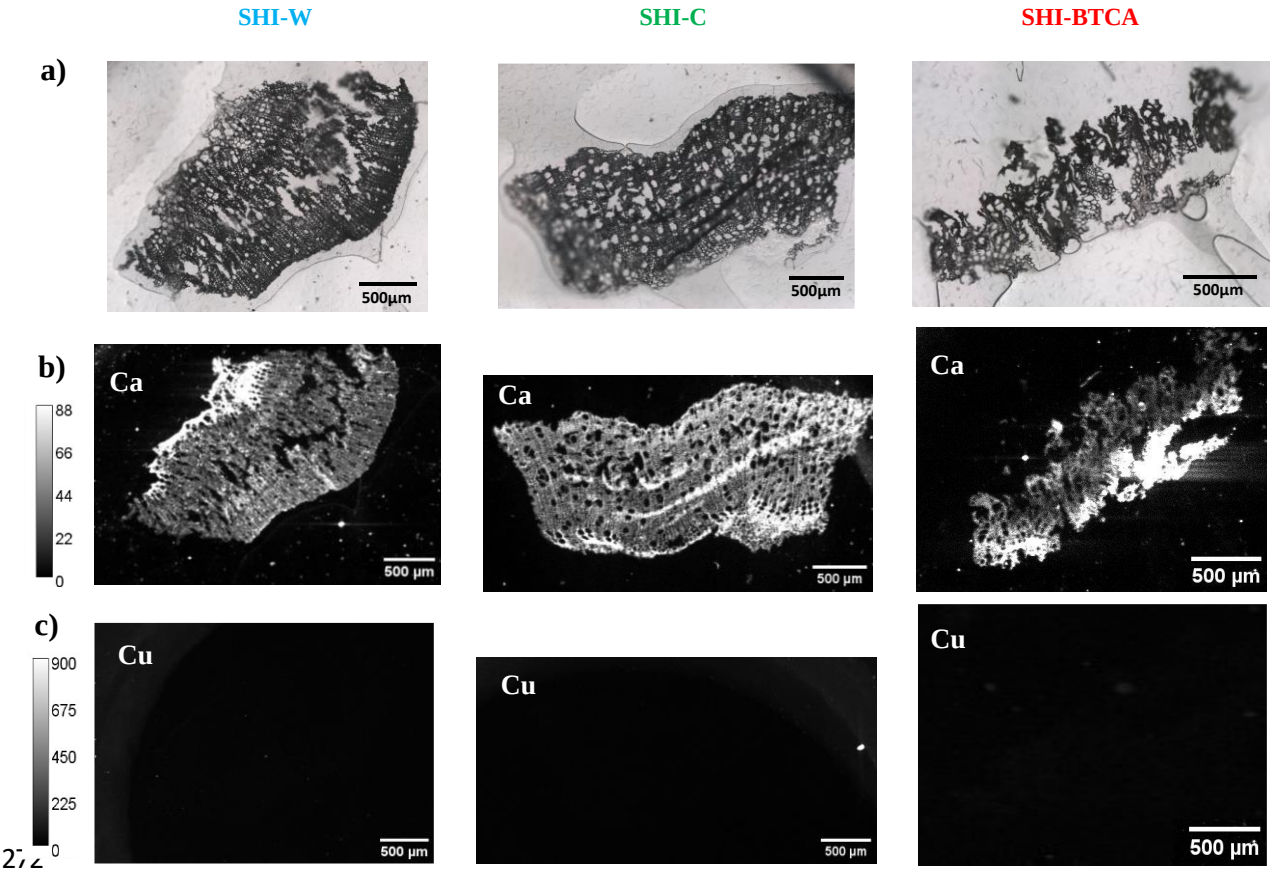

Fig. 5 Comparison of transverse sections of SHI-W, SHI-C and SHI-BTCA samples before copper adsorption obtained by a) optical microscopy, b) synchrotron-based XRF mapping of Ca, and c) synchrotron-based XRF mapping of Cu. For a given element, the grey scale of the XRF images is the same for the three samples.

After adsorption, all samples show the presence of the copper fluorescence signal. The images of Figures 6, 7 and 8 show the maps of Cu and Ca recorded for transverse sections at different depths for, respectively, SHI-WCu, SHI-CCu and SHI-BTCACu shives. A comparison of these maps reveals the following: (i) The fluorescence intensity of Cu is lower in SHI-WCu than in SHI-CCu and SHI-BTCACu, in agreement with published results on the removal of Cu present in contaminated solutions (Mongioví et al. 2022b); (ii) In the SHI-WCu and SHI-CCu samples, Cu is distributed over all the free surface, internal and external, with no obvious preferential accumulation areas; These images are therefore in agreement with the results of micro-tomography and with the hypothesis of a mechanism dominated by diffusion; (iii) For SHI-BTCACu, a different copper distribution is observed depending on the depth of the cross-section observed. In particular, for the most superficial or external section (Figure 8a), Cu seems to be distributed over the entire surface while, for the inner section (Figure 8b), the metal is rather located at the periphery of the sample; this observation is in agreement with the results of micro-tomography, confirming the hypothesis of phenomena such as ion exchange or microprecipitation. Supplementary data also presents maps obtained on other transverse and longitudinal sections which confirm the observations described above, such as the lower amounts of adsorbed Cu for SHI-WCu than for SHI-CCu and SHI-BTCA-Cu.

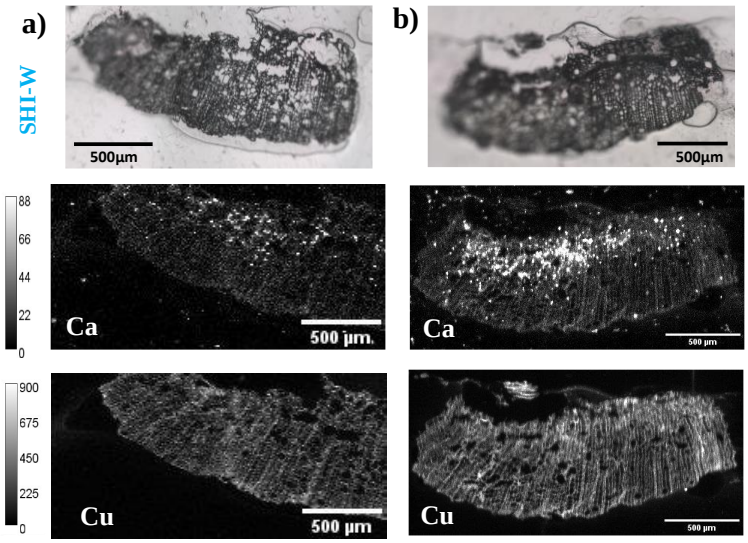

Fig. 6 Optical microscope images (top) and X-ray fluorescence maps of Ca (middle) and Cu (bottom) for two SHI-WCu transverse sections. The sections are obtained at two different depths of the same hemp shives a superficial cross-section (a) and an internal cross-section (b). For a given element, the gray scale of the XRF maps (in number of normalized shots) is the same for all samples and is identical to the previous figure.

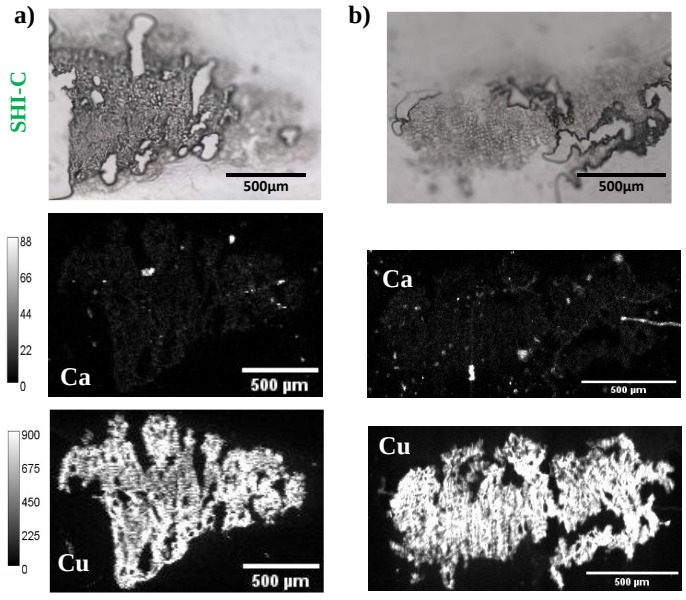

Fig. 7 Optical microscope images (top), X-ray fluorescence maps of Ca (middle), and Cu (bottom) of two SHI-CCu transverse sections. The sections are obtained at two different depths of the same hemp shive, a superficial cross-section (a) and an internal cross-section (b). For a given element, the gray scale of the XRF maps (in number of normalized counts) is the same for all samples and is identical to the previous figures.

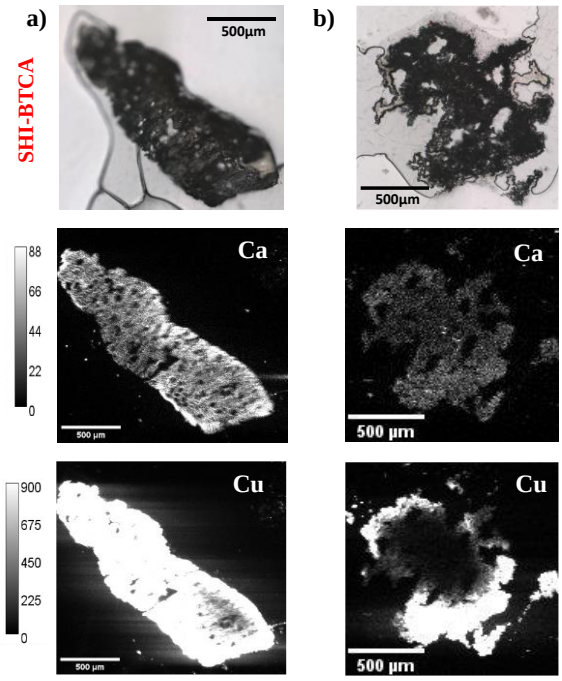

307

308 **Fig. 8** Optical microscope images (top), X-ray fluorescence maps of Ca (middle), and Cu (bottom)
309 for the two SHI-BTCACu transverse sections. The sections are obtained at two different depths of
310 the same hemp shive, a superficial cross-section (a) and an internal cross-section (b). For a given
311 element, the gray scale of the XRF maps (in number of normalized counts) is the same for all
312 samples and is identical to the previous figures.

313 The data analysis made it possible to carry out a statistical study of the distribution of
314 fluorescence intensities in the XRF maps and thus of the distribution of copper. Two types
315 of analysis were performed: the first is the extraction of a Cu distribution profile along a
316 15-pixel-thick line passing through the sample in the radial direction, and the second is
317 the determination of the average copper value (in terms of fluorescence intensity) over
318 the entire surface of the sample. Figure 9 shows the Cu distribution profiles extracted
319 from µ-XRF maps for internal transverse sections. In Figures 9b and 9d, it can be seen that,
320 for SHI-WCu and SHI-CCu samples, the signal is present throughout the area analyzed. The
321 metal appears to be distributed evenly in the washed sample, with intensities between
322 200 and 400 counts on the scale (Figure 9b). The SHI-C profile shows signals with higher
323 intensities (values between 600 and 1000 counts, as opposed to 200 to 400 for SHI-WCu)
324 except for the area around 100 µm, where excessive degradation of the sample structure
325 led to lower Cu presence and therefore a decrease in the signal (Figure 9d). Concerning
326 the SHI-BTCACu sample, it can be seen that, for the inner transverse section, the
327 distribution profile of copper is totally different from that in SHI-WCu and SHI-CCu,
328 characterized on the one hand by two areas of high intensity (between 1500 and 3000
329 counts) in the most external parts of the section and, on the other hand, the absence of
330 signal in the inner part, between 250 and 550 µm (Figure 9f).

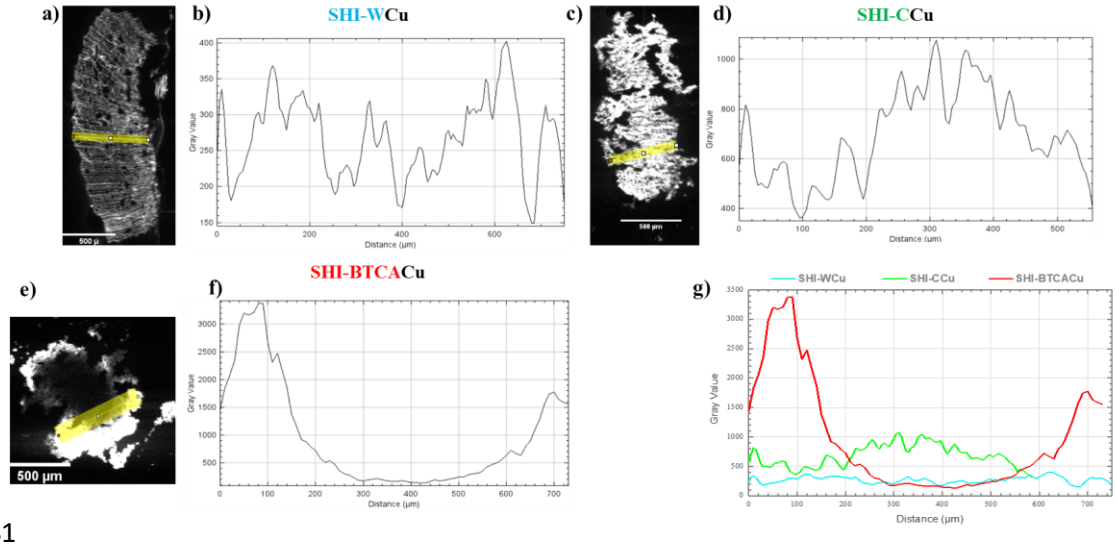

331

332 **Fig. 9** XRF fluorescence maps of the Cu element (a, c and e) and Cu distribution profiles (b, d and
333 f) extracted from internal sections of SHI-WCu, SHI-CCu and SHI-BTCACCu shives, and comparison
334 of the profile intensity of the three materials (g). The location of the profile is shown in yellow on
335 the fluorescence maps.

336 For the external transverse sections of SHI-WCu and SHI-CCu samples (Figure 10), the
337 profiles plotted do not differ significantly from those of the internal sections (Figure 10b
338 and Figure 10d, respectively). For the SHI-BTCACu sample, two different areas were
339 analyzed. The first shows that copper is distributed throughout the analyzed area (Figure
340 10f) while, for the second, the Cu distribution profile shows a pattern similar to that of
341 the inner section, with external peaks of very high intensity (up to 20000 counts) and a
342 central zone with a very low signal (Figure 10h).

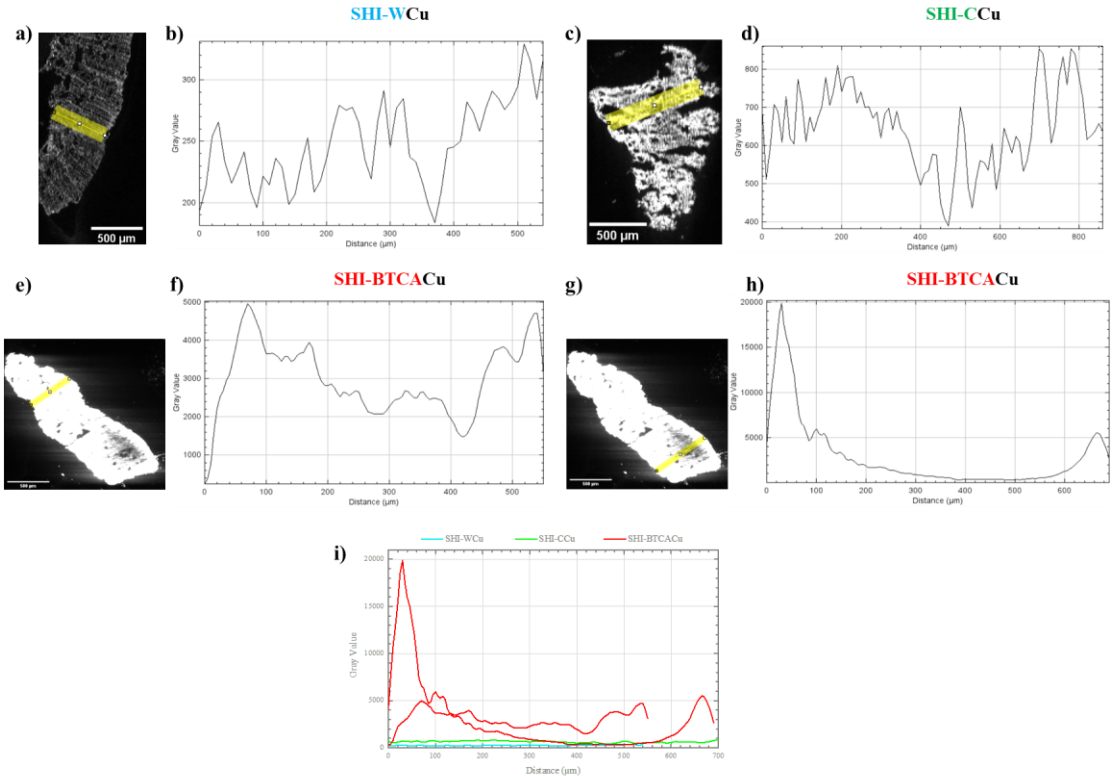

343

Fig. 10 XRF maps of Cu (a, c, e, g) and Cu distribution profiles (b, d, f, h) extracted from superficial sections of SHI-WCu, SHI-CCu and SHI-BTCACu shives, and comparison of the profile intensity of the three materials (i). The location of the profiles is shown in yellow on the fluorescence maps.

Finally, Figure 11 shows the average Cu intensity values calculated by analyzing the area of three transverse sections of each sample. For SHI-WCu and SHI-CCu, Cu distribution on the sur-face is more homogeneous and comparable from one section to another, since the values are similar with lower standard deviations, compared to SHI-BTCA. This distribution is in accordance with a diffusion mechanism. In addition, if we compare SHI-WCu and SHI-CCu samples, the amounts of Cu present in the transverse sections are greater for SHI-CCu. It can therefore be concluded that the distribution of copper on the surface depends on the structure of the sample and therefore on the treatment undergone (to be related to the different degradation and chemical composition for the two samples).

For SHI-BTCACu, there is a large variation in both mean copper values and standard deviations. This result can be explained if we consider that the distribution of copper depends on the area of contact with the adsorbent during adsorption experiments. This observation is consistent with a grafting of non-homogeneous BTCA ligands over the entire surface, and consequently, the existence of preferential areas of interaction between Cu and these functions.

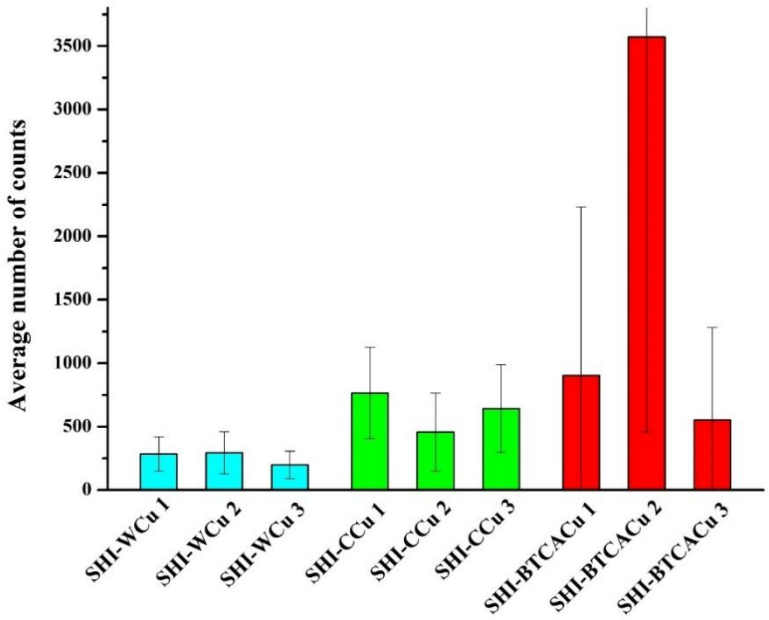

Fig. 11 Average copper fluorescence intensity values (number of counts) for SHI-WCu, SHI-CCu and SHI-BTCACu samples obtained by analyzing three different transverse sections.

Conclusion

In this work, the spatial distribution of the copper complexed by three hemp shives has been determined by a combination of K-edge subtraction micro-tomography and X-ray micro-fluorescence imaging. These two synchrotron techniques are complementary as tomography provides 3D information but is less sensitive to elemental concentrations,

while X-ray fluorescence imaging allows for a lower detection limit but only provides 2D information. Both techniques confirmed that the Cu distribution is totally different for the three samples. For SHI-W and SHI-C, Cu is present both in the internal and external surface of the adsorbent while for SHI-BTCA, it is mainly localized at the surface where carboxylic groups are present. The observations corroborate a diffusion mechanism for SHI-W and SHI-C and a chemisorption mechanism for SHI-BTCA during the solid-liquid adsorption experiments involving hemp adsorbents and copper present in monocontaminated solutions. To continue this work, we will use the same techniques to study the interactions between the same materials and metals present in polycontaminated solutions.

Acknowledgements

Grégorio Crini thanks Eurochanvre (Arc-les-Gray, France) for the gift of the materials. Chiara Mongioví thanks the Région Bourgogne Franche-Comté for awarding her a research grant. The authors acknowledge Synchrotron SOLEIL for providing beamtime (proposal 20220289). ANATOMIX is an Equipment of Excellence (EQUIPEX) funded by the Investments for the Future program of the French National Research Agency (ANR), project NanoimagesX, grant no. ANR-11-EQPX-0031.

Funding

The authors thank the *Région Bourgogne Franche-Comté* and *Université de Franche-Comté* (FINEAU project 2020-2024) for financial support. This work has also been supported by the EIPHI Graduate School (contract ANR-17-EURE-0002).

Author contributions

CM, XG, JG, WA, MC, JP, TW, SD, LB, CR, SC, KM: Conducting experiments, analysing and interpreting data, data curation, software. JB, VP and GC: Validation. CM, XG, CR, JB, VP and GC: Conceptualization, methodology, validation, supervision. CM and GC: writing original draft, review and editing. GC: Resources, funding acquisition, project administration. All the authors have given approval to the final version of the manuscript.

Declarations

Supplementary Information

The online version contains supplementary material available at.

Conflict of interest

The authors declare that they have no known competing financial interests or personal relationships that could have appeared to influence the work reported in this paper.

Informed consent

All the authors have provided their consent for the submission of the presented work.

References

Ahmed E, Zeitoun A, Hamad G, Zeitoun MAM, Taha A, Korma SA, Esatbeyoglu T (2022) Lignocellulosic biomasses from agricultural wastes improved the quality and physicochemical properties of frying oils. Foods 11:3149. https://doi.org/10.3390/foods11193149

Akköz Y, Coşkun R (2023) Preparation of highly effective bio-adsorbent from hemp fiber for removal of malachite green oxalate (MGO). Cellulose 30:4511-4525. https://doi/10.1007/s10570-023-05167-y

Asberry HB, Kuo CY, Gung CH, Conte ED, Suen SY (2014) Characterization of water bamboo husk biosorbents and their application in heavy metal ion trapping. Microchem J 113:59-63. https://doi.org/10.1016/j.microc.2013.11.011

Basnet P, Gyawali D, Ghimire KN, Paudyal H (2022) An assessment of the lignocellulose-based biosorbents in removing Cr(VI) from contaminated water: A critical review. Results Chem 4:100406. https://doi.org/10.1016/j.rechem.2022.100406

Biziks V, Van den Bulcke J, Grinins J, Militz H, Andersons B, Andersone I, Dhaene J, Van Acker J (2016) Assessment of wood microstructural changes after one-stage thermo-hydro treatment (THT) by micro-X-ray computed tomography. Holzforschung 70:167-177. https://doi.org/10.1515/hf-2014-0337

Chandraghatgi R, Englezos T (2008) Sequestering of heavy metal ions from aqueous solutions by using a lignocellulosic material. Int J Environ Pollut 32:509-518. https://doi.org/10.1504/IJEP.2008.018414

Crini G, Bradu C, Cosentino C, Staelens JN, Martel B, Fourmentin M, Loiacono S, Chanet G, Torri G, Morin-Crini N (2021) Simultaneous removal of inorganic and organic pollutants from polycontaminated wastewaters on modified hemp-based felts. Rev Chim 72:25-43. https://doi.org/10.37358/Rev.Chim.1949

Cruz-Lopes L, Macena M, Esteves B, Santos-Vieira I (2022) Lignocellulosic materials used as biosorbents for the capture of nickel (II) in aqueous solution. Appl Sci 12:933. https://doi.org/10.3390/app12020933

da Rocha Rodrigues EJ, Cucinelli Neto RP, Lopes Alves HD, Paciornik S, Santos de Sá D, Ghavami K, Pandoli OG (2023) An investigation of the fluid-holding cavities in a lignocellulosic-based bamboo matrix via a combined X-Ray microtomography and proton time-domain NMR approach. Cellulose 30:4925-4940. https://doi-org/10.1007/s10570-023-05197-6

de Quadros Melo D, de Oliveira Sousa Neto V, de Freitas Barros FC, Cabral Raulino GS, Bastos Vidal C, do Nascimento RF (2016) Chemical modifications of lignocellulosic materials and their application for removal of cations and anions from aqueous solutions. J Appl Polym Sci 133:43286. https://doi.org/10.1002/app.43286

Desjardins K, Scheel M, Giorgetta JL, Weitkamp T, Menneglier C, Carcy A (2018) Design of indirect X-ray detectors for tomography on the ANATOMIX beamline. Proc. 10th Mechanical Engineering Design of Synchrotron Radiation Equipment and Instrumentation (MEDSI 2018), pp. 355-357. https://doi.org/10.18429/JACoW-MEDSI2018-THPH09

Furlan FL, Consolin N, Consolin MFB, Gonçalves MS, Valderrama P, Genena AK (2018) Use of agricultural and agroindustrial residues as alternative adsorbents of manganese and iron in aqueous solution. Rev. Ambiente Água 13:1-13. https://doi.org/10.4136/ambi-agua.2181

Halysh V, Sevastyanova O, Pikus S, Dobele G, Pasalskiy B, Gun'ko M, Kartel M (2020) Sugarcane bagasse and straw as low-cost lignocellulosic sorbents for the removal of dyes and metal ions from water. Cellulose 27:81-8197. https://doi/10.1007/s10570-020-03339-8

Jiang Y, Ansell MP, Jia X, Hussain A, Lawrence M (2017) Physical characterization of hemp shiv: cell wall structure and porosity. Academic J Civ Eng 35:22-28. https://doi.org/10.26168/icbbm2017.1

Jiang Y, Lawrence M, MP Ansell, Hussain A (2018) Cell wall microstructure, pore size distribution and absolute density of hemp shiv. R Soc Open Sci 5:171945. https://doi.org/10.1098/rsos.171945

Junior ACG, Strey L, Lindino CA, Nacke H, Schwantes D, Seidel EP (2012) Applicability of the Pinus bark (*Pinus elliottii*) for the adsorption of toxic heavy metals from aqueous solutions. Acta Sci Technol 34:79-87. https://doi.org/10.4025/actascitechnol.v34i1.95

Lee BG, Rowell RM (2004) Removal of heavy metal ions from aqueous solutions using lignocellulosic fibers. J Nat Fibers 1:97-108. https://doi.org/10.1300/J395v01n01_07

Maceda A, Terrazas T (2022) Fluorescence microscopy methods for the analysis and characterization of lignin. Polymers. 14:961. https://doi.org/10.3390/polym14050961.

Müller D, Graetz J, Balles A, Stier S, Hanke R, Fella C (2021) A novel nano-tomography setup for material science and engineering applications, Cornell University. https://doi.org/10.48550/arXiv.2102.06644

Mergbi M, Galloni MG, Aboagye D, Elimian E, Su PD, Ikram BM, Nabgan W, Bedai J, Amor HB, Contreras S, Median F, Djellabi R (2023) Valorization of lignocellulosic biomass into sustainable materials for adsorption and photocatalytic applications in water and air remediation. Environ Sci Pollut Res 30:74544-74574. https://doi.org/10.1007/s11356-023-27484-2

Mirone A, Brun E, Gouillart E, Tafforeau P, Kieffer J (2014) The PyHST2 hybrid distributed code for high speed tomographic reconstruction with iterative reconstruction and a priori knowledge capabilities. Nucl Instrum Methods Phys Res B 324:41-48. https://doi.org/10.1016/j.nimb.2013.09.030

Mokgehle TM, Tavengwa NT (2021) Recent developments in materials used for the removal of metal ions from acid mine drainage. Appl Water Sci 11:42. https://doi.org/10.1007/s13201-020-01350-9

Mongioví C, Crini G (2023) Copper recovery from aqueous solutions by hemp shives: Adsorption studies and modeling. Processes. 11:191. https://doi.org/10.3390/pr11010191

Mongioví C, Lacalamita D, N Morin-Crini, Gabrion X, Ivanovska A, Sala F, Placet V, Rizzi V, Gubitosa J, Mesto E, Ribeiro ARL, Fini P, Vietro ND, Schingaro E, Kostić M, Cosentino C, Cosma P, Bradu C, Chanet G, Crini G (2021) Use of chènevotte, a valuable co-product of industrial hemp fiber, as adsorbent for pollutant removal. Part I: Chemical, microscopic, spectroscopic and thermogravimetric characterization of raw and modified samples. Molecules 26:4574. https://doi.org/10.3390/molecules26154574

Mongioví C, Crini G, Gabrion X, Placet V, Blondeau-Patissier V, Krystianiak A, Durand S, Beaugrand J, Dorlando A, Rivard C, Gautier L, Ribeiro ARL, Lacalamita D, Martel B, Staelens JN, Ivanovska A,

Kostić M, Heintz O, Bradu C, Raschetti M, Morin-Crini N (2022a) Revealing the adsorption mechanism of copper on hemp-based materials through EDX, nano-CT, XPS, FTIR, Raman, and XANES characterization techniques. Chem Eng J Adv 10:100282. https://doi.org/10.1016/j.ceja.2022.100282

Mongioví C, Lacalamita D, Morin-Crini N, Gabrion X, Placet V, Ribeiro ARL, Ivanovska A, Kostić M, Bradu C, Staelens JN, Martel B, Raschetti M, Crini G (2022b) Use of chènevotte, a valuable co-product of industrial hemp fiber, as adsorbent for copper ions: Kinetic studies and modeling. Arabian J Chem 15:103742. https://doi.org/10.1016/j.arabjc.2022.103742

Morin-Crini N, Loiacono S, Placet V, Torri G, Bradu C, Kostić M, Cosentino C, Chanet G, Martel B, Lichtfouse E, Crini G (2019) Hemp-based adsorbents for sequestration of metals: A review. Environ Chem Lett 17:393-408. https://doi.org/10.1007/s10311-018-0812-x

Morin-Crini N, Staelens JN, Loiacono S, Martel B, Chanet G, Crini G (2020) Simultaneous removal of Cd, Co, Cu, Mn, Ni and Zn from synthetic solutions on a hemp-based felt. III. Real discharge waters. J Appl Polym Sci 137:48823. https://doi.org/10.1002/app.48823

Pinsard L, Revol N, Pomikal H, De Luycker E, Ouagne P (2023) Production of long hemp fibers using the flax value chain. Fibers. 11: 38. https://doi.org/10.3390/fib11050038

Santander P, Butter B, Oyarce E, Yáñez M, Xiao LP, Sánchez J (2021) Lignin-based adsorbent materials for metal ion removal from wastewater: A review. Ind Crops Prod 167:113510. https://doi.org/10.1016/j.indcrop.2021.113510

Scheel M, Perrin J, Koch F, Daniel G, Giorgetta J, Cauchon G, King A, Yurgens V, Le Roux V, David C, Weitkamp T (2022) Current status of hard X-ray nano-tomography on the transmission microscope at the ANATOMIX beamline. J Phys Conf Ser 2380:012045. https://doi.org/10.1088/1742-6596/2380/1/012045

Sharma A, Anjana, Rana H, Goswami S (2022) A comprehensive review on the heavy metal removal for water remediation by the application of lignocellulosic biomass-derived nanocellulose. J Polym Environ 30:1-18. https://doi.org/10.1007/s10924-021-02185-4

Shen XP, Xie YJ, Wang QW, Yi X, Shamshina JL, Rogers RD (2019) Enhanced heavy metal adsorption ability of lignocellulosic hydrogel adsorbents by the structural support effect of lignin. Cellulose 26:1005-4019. https://doi.org/10.1007/s10570-019-02328-w

Sjahro N, Yunus R, Abdullah LC, Rashid SA, Asis AJ, Akhlisah ZN (2021) Recent advances in the application of cellulose derivatives for removal of contaminants from aquatic environments. Cellulose 28:7521-7557. https://doi/10.1007/s10570-021-03985-6

Solé VA, Papillon E, Cotte M, Walter P, Susini J (2007) A multiplatform code for the analysis of energy-dispersive X-ray fluorescence spectra. Spectrochim Acta Part B 62:63-68. https://doi.org/10.1016/j.sab.2006.12.002

Sun Q, Xia YD, Klinger J, Seifert R, Kane J, Thompson V, Chen QS (2021) X-ray computed tomography-based porosity analysis: Algorithms and application for porous woody biomass. Powder Technol 388:496-504. https://doi.org/10.1016/j.powtec.2021.05.006

Thompson AC, Kirz J, Attwood DT, Gullikson EM, Howells MR, Kortright JB, YW Liu, Robinson AL, Under-wood JH, Kim KJ, Lindau I, Pianetta P, Winick H, Williams GP, Scofield JH. (2009) X-Ray Data Booklet. Lawrence Berkeley National Laboratory, University of California, Berkeley CA 94720

Weitkamp T, Scheel M, Perrin J, Daniel G, King A, Le Roux V, Giorgetta J, Carcy A, Langlois F, Desjardins K, Menneglier C, Cerato M, Engblom C, Caucon G, T Moreno, Rivard C, Y Gohon, Polack F (2022) Microtomography on the ANATOMIX beamline at Synchrotron SOLEIL. J Phy Conf Ser 2380:012122. https://doi.org/10.1088/1742-6596/2380/1/012122

532 Wang D (2019) A critical review of cellulose-based nanomaterials for water purification in industrial
533 processes. Cellulose 26:687-701. https://doi/10.1007/s10570-018-2143-2

534 Zeng H, Su YM, Gong X, Zheng LC, Zhang LJ, Meng PP, Zhou QY, Ren JJ (2023) Competitive
535 adsorption behavior of typical heavy metal ions from acid mine drainage by
536 multigroup-functionalization cellulose: qualitative and quantitative mechanism. Environ Sci Pollut
537 Res 30:68191-68205. https://doi.org/10.1007/s11356-023-27188-7